Acta Cryst. (1970). A26, 315

Self-Crystallizing Molecular Models. III

BY TARO KIHARA

Department of Physics, Faculty of Science, University of Tokyo, Tokyo, Japan

(*Received* 13 *June*, 1969)

Structures of typical molecular crystals are simulated in a 'quantitative' way by the use of molecular models composed of two kinds of ferrite: one is magnetized barium ferrite and the other is a manganese–zinc ferrite of high permeability. These two components represent the permanent electric multipole and the electric polarizability of a molecule, respectively. On the basis of these molecular models, some predictions are made as to the unestablished crystal structures. The low temperature modification of C_2H_2 is probably either *Pnnm* (D_{2h}^{12}) or *Cmca* (D_{2h}^{18}). The lowest-temperature forms of CH_4 and CD_4 are probably in the space groups $I\bar{4}2m$ (D_{2d}^{11}), $P4_2/nmc$ (D_{4h}^{18}), *Pban* (D_{2h}^{4}) or $C2/c$ (C_{2h}^{6}). The crystal structure of OsF_8 is probably $R\bar{3}$ (C_{3i}^{2}).

The structure of a molecular crystal is governed by the shape of the molecules as well as by the intermolecular force, which depends on the mutual orientation of the molecules. The purpose of this series of papers is to establish, by the use of molecular models, the relation between these molecular characteristics and the crystal structure.

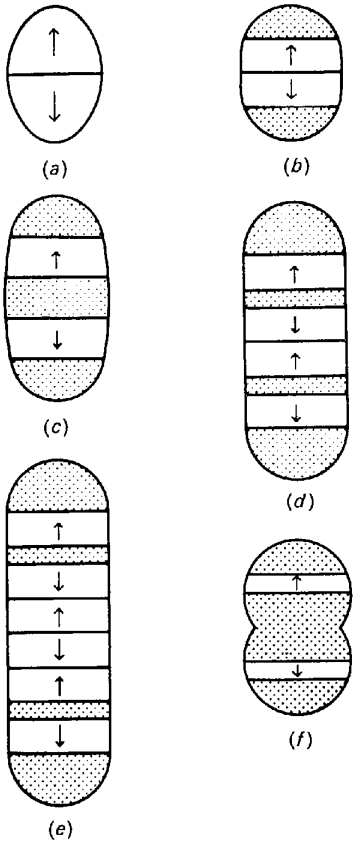

Fig. 1. Models of slender molecules. (*a*) Model 1*a*, a quadrupolar spheroid. (*b*) Model 1*b*, a quadrupolar spheroid with polarizability. (*c*) Model 1*c* for N≡C–C≡N, $ClCH_2CH_2Cl$, *etc.* (*d*) Model 1*d* for N≡C–C≡C–C≡N. (*e*) Model 1*e* for CH_3–C≡C–C≡C–C≡C–CH_3. (*f*) Model 1*f* for Cl_2, Br_2 and I_2. Manganese–zinc ferrite is shaded with dots.

The models simulate magnetically the electric forces between actual molecules: they consist of barium-ferrite magnets and manganese–zinc ferrite pieces arranged in such a way that the electric multipole and the electric polarizability of each molecule are represented by the magnetic multipole and the magnetic susceptibility of the model, respectively. Here the Mn–Zn ferrite pieces, whose permeability is greater than 1000, are not permanently magnetized but magnetization is induced in these pieces by the 'hard' Ba-ferrite magnets when they are brought close enough; thus the effect of induced polarization of a molecule is represented. When the shape and magnetic property of a model are arranged to simulate a given molecule, a structure into which these models are assembled will simulate the actual crystal structure.

The principles upon which our molecular models are based are 'simplicity', 'generality' and 'accuracy'. The shape of a model is chosen to be as simple as possible, inessential details of the actual molecular shape being neglected. For example, our model of the benzene molecule is axially symmetric showing that the deviation of the actual molecular shape from axial symmetry is not essential to the crystal structure. It is desired that a variety of general characteristics of the structures of molecular crystals can be clarified by this method. Finally, the structures formed by the models should be reasonably accurate.

In particular cases, the polarizability of the molecule does not play an essential part in determining the crystal structure. Such cases were dealt with in parts I and II* (Kihara, 1963, 1966). The models, however, are greatly improved by using both types of ferrite. A molecule with large polarizability but relatively small multipole moment cannot be represented by a model made of Ba ferrite magnets only. Examples are Cl_2, BCl_3, SiI_4, B_4Cl_4, *etc.*

* Erratum: in part II Figs. 15 and 16 should be interchanged.

On the basis of these molecular models, some predictions are made on crystal structures which have not been established.

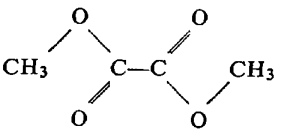

Slender molecules

The molecular models 1*a*–1*d*, shown in Fig. 1, represent the crystal structures of typical slender molecules:

carbon dioxide O=C=O,
acetylene H–C≡C–H,
cyanogen N≡C–C≡N,
dimethylacetylene CH_3–C≡C–CH_3,
1,2-dichloroethane Cl–CH_2–CH_2–Cl,
trans-1,4-dibromocyclohexane

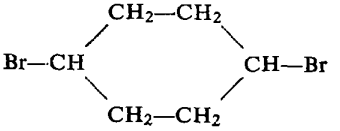

dicyanoacetylene N≡C–C≡C–C≡N,
dimethyltriacetylene CH_3–C≡C–C≡C–C≡C–CH_3,
heavy halogens Cl_2, Br_2, I_2, and
dimethyl oxalate $(COOCH_3)_2$,

The crystal structures are compared in Table 1 with corresponding arrangements formed by the models; most of these arrangements are shown in Figs. 2–8.

The crystal structure of acetylene below the transition temperature of −140°C is orthorhombic and belongs to the holohedral class *mmm* (D_{2h}), the molecules being located at sites of 2/*m* (C_{2h}) symmetry (Sugawara & Kanda, 1952; Bottger & Eggers, 1964; Ito, Yokoyama & Suzuki, 1969).

The molecule of acetylene is simulated by the model 1*b*, which is a quadrupolar spheroid with Mn–Zn ferrite caps. Two orthorhombic structures can be formed by this model: *Pnnm* (D_{2h}^{12}) with two molecules in a unit cell and *Cmca* (D_{2h}^{18}) with four molecules in a unit cell, as shown in Figs. 3 and 4. In these two structures, the molecules are at sites of 2/*m* symmetry.

Furthermore, the cubic *Pa*3 structure, which is stable above −140°C, is readily transformed to either of these orthorhombic structures. [It should be noted that only the *Pa*3 structure can be formed by the model of quadrupolar spheres (see parts I and II), and the effective shape of the molecule in crystalline C_2H_2 at

Table 1. *Slender molecules*

CO_2	*Pa*3 (T_h^6)	$Z=4$*				(IV, i1)†
N_2 below 35°K	*Pa*3 (T_h^6)	$Z=4$				(II, j2)
C_2H_2 above −140°C	*Pa*3 (T_h^6)	$Z=4$				(XIV, b29)
C_2H_2 below −140°C	crystal class	*mmm* (D_{2h})				
models 1*a* and 1*b*	*Pa*3 (T_h^6)	$Z=4$				Fig. 2
models 1*a* and 1*b*	*Pnnm* (D_{2h}^{12})	$Z=2$	$a/c=0{\cdot}7$	$b/c=0{\cdot}9$		Fig. 3
model 1*b*	*Cmca* (D_{2h}^{18})	$Z=4$	$a/c=0{\cdot}85$	$b/c=0{\cdot}85$		Fig. 4
$(CN)_2$	*Pbca* (D_{2h}^{15})	$Z=4$	$a/c=0{\cdot}874$	$b/c=0{\cdot}891$		(XIV, b2)
CH_3–C≡C–CH_3 above −119°C	$P4_2/mnm$ (D_{4h}^{14})	$Z=2$	$c/a=1{\cdot}27$			(XIV, b30)
$ClCH_2CH_2Cl$	$P2_1/c$ (C_{2h}^5)	$Z=2$	$a/b=0{\cdot}860$	$c/b=1{\cdot}454$	$\beta=103°30'$	(−140°C)
			$a/b=0{\cdot}906$	$c/b=1{\cdot}439$	$\beta=109°30'$	(−50°C)
	Above −96°C the molecule is rotating about its Cl–Cl axis					XIV, b4)
trans-1,4-dibromocyclohexane	$P2_1/c$ (C_{2h}^5)	$Z=2$	$a/b=1{\cdot}083$	$c/b=2{\cdot}144$	$\beta=101°49'$	(C.D.)‡
trans-1,4-dichlorocyclohexane and *trans*-1,4diiodocyclohexane are similar						
model 1*c*	*Pbca* (D_{2h}^{15})	$Z=4$	$a/c=0{\cdot}85$	$b/c=0{\cdot}85$		Fig. 5
	$P4_2/mnm$ (D_{4h}^{14})	$Z=2$	$c/a=1{\cdot}27$			
	$P2_1/c$ (C_{2h}^5)	$Z=2$	$a/b=1{\cdot}0$	$c/b=1{\cdot}8$	$\beta=100°$	
N≡C–C≡C–C≡N	$P2_1/c$ (C_{2h}^5)	$Z=2$	$a/b=0{\cdot}639$	$c/b=1{\cdot}478$	$\beta=99°20'$	(XIV, b32)
model 1*d*	$P2_1/c$ (C_{2h}^5)	$Z=2$	$a/b=0{\cdot}65$	$c/b=1{\cdot}70$	$\beta=100°$	Fig. 6
CH_3–C≡C–C≡C–C≡C–CH_3	$R\bar{3}m$ (D_{3d}^5)	$Z=1$	$\alpha=70°58'$			(XIV, b33)
model 1*e*	$R\bar{3}m$ (D_{3d}^5)	$Z=1$	$\alpha=70°$			Fig. 7
Cl_2	*Cmca* (D_{2h}^{18})	$Z=4$	$a/c=0{\cdot}755$	$b/c=0{\cdot}524$		(II, u)
Br_2	*Cmca* (D_{2h}^{18})	$Z=4$	$a/c=0{\cdot}765$	$b/c=0{\cdot}514$		(II, u)
I_2	*Cmca* (D_{2h}^{18})	$Z=4$	$a/c=0{\cdot}742$	$b/c=0{\cdot}490$		(II, u)
$(COOCH_3)_2$						
model 1*f*	$P2_1/n$ (C_{2h}^5)	$Z=2$	$a/b=0{\cdot}328$	$c/b=0{\cdot}523$	$\beta=103°$	(XIV, b124)
	Cmca (D_{2h}^{18})	$Z=4$	$a/c=0{\cdot}60$	$b/c=0{\cdot}50$		Fig. 8
	$P2_1/n$ (C_{2h}^5)	$Z=2$	$a/b=0{\cdot}51$	$c/b=0{\cdot}69$	$\beta=95°$	

* Z denotes the number of molecules in a unit cell.
† IV, i1 stands for Chapter IV, i1 in Wyckoff (1963, 1964, 1966).
‡ C.D. stand for *Crystal Data* by Donnay, Donnay, Cox, Kennard & King (1963).

Fig. 2. Cubic *Pa*3 structure simulating the crystal structure of carbon dioxide (model 1*b*).

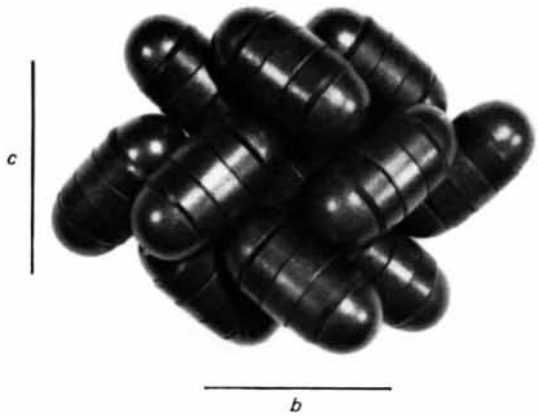

Fig. 5. Orthorhombic *Pbca* structure simulating the crystal structure of cyanogen (model 1*c*).

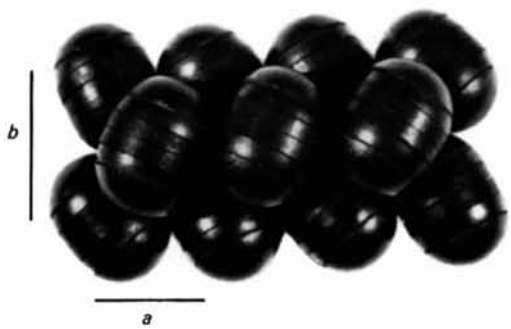

Fig. 3. Orthorhombic *Pnnm* structure (model 1*b*).

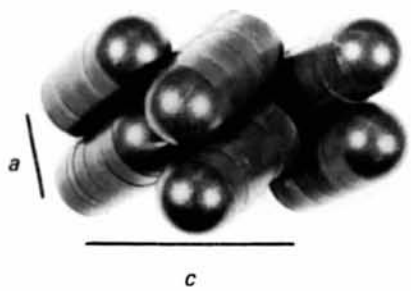

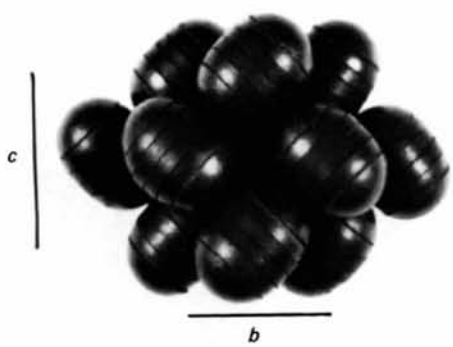

Fig. 4. Orthorhombic *Cmca* structure (model 1*b*).

Fig. 6. Monoclinic $P2_1/c$ structure simulating the crystal structure of dicyanoacetylene (model 1*d*).

[*To face p.* 316

Fig. 7. Rhombohedral $R\bar{3}m$ structure simulating the crystal structure of dimethyltriacetylene (model 1*e*).

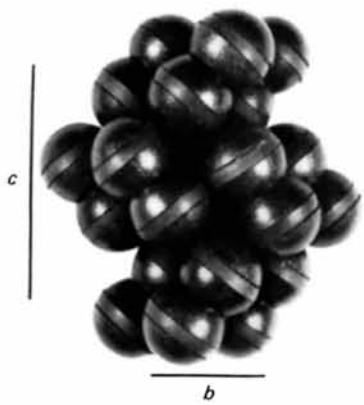

Fig. 8. Orthorhombic *Cmca* structure simultaing the crystal structure of chlorine, bromine and iodine (model 1*f*).

Fig. 10. Cubic *Im*3 structure simulating the crystal structure of N_2O_4 (model 2*d*).

Fig. 11. Hexagonal $P6_3/m$ structure simulating the crystal structure of BCl_3, BBr_3 and BI_3 (Model 2*e*).

Fig. 13. Cubic $I\bar{4}3m$ structure simulating the crystal structure of SiF_4 (model 3*b*).

Fig. 14. Cubic *Pa*3 structure simulating the crystal structure of SiI_4, GeI_4, SnI_4, *etc.* (model 3*c*).

high temperatures is more like a sphere than at low temperatures, owing to thermal motions.]

Hence it is highly probable that either the *Pnnm* or *Cmca* structure corresponds to the actual crystal structure of acetylene below −140° C. (In part II, the author predicted the *Pnnm* structure on the basis of the packing of barium-ferrite spheroids. On the other hand, Ito, Yokoyama & Suzuki (1969) concluded that the *Cmca* structure is the most probable; this conclusion is based on Sugawara's inference that there are four molecules in a unit cell.)

Flat molecules

The molecular models 2*a*–2*e*, which are shown in Fig. 9, represent the crystal structures of typical flat molecules:

β-hexachlorocyclohexane $C_6H_6Cl_6$,
β-hexabromocyclohexane $C_6H_6Br_6$,
benzene C_6H_6,
naphthalene
anthracene

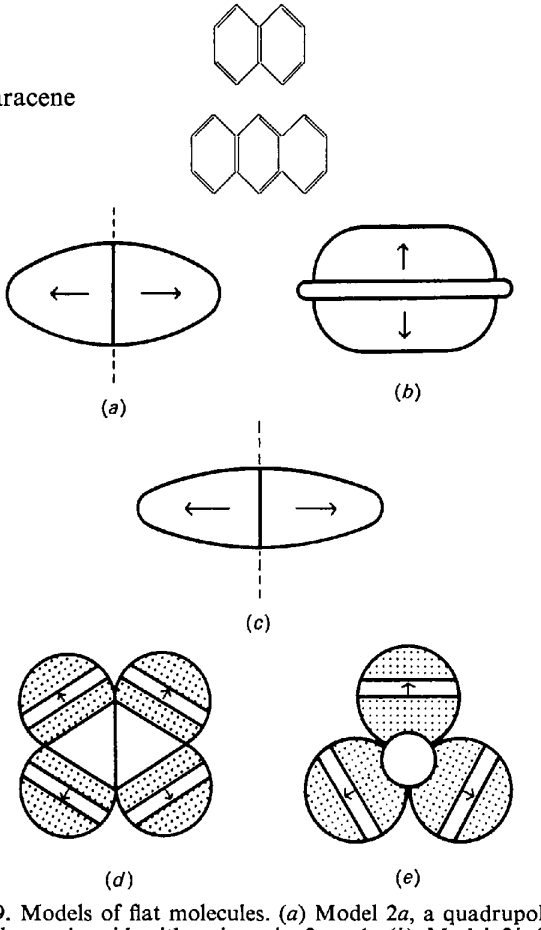

Fig. 9. Models of flat molecules. (*a*) Model 2*a*, a quadrupolar oblate spheroid with axis ratio 2 to 1. (*b*) Model 2*b* for benzene; the thin disk between the two magnets is made of plastic. (*c*) Model 2*c*, a quadrupolar oblate spheroid with the axis ratio 3 to 1. (*d*) Model 2*d* for N_2O_4. (*e*) Model 2*e*, for BCl_3, BBr_3, and BI_3; the central sphere representing the boron atom is made of plastic.

tetracyanoethylene $(CN)_2C=C(CN)_2$,
dinitrogen tetroxide N_2O_4,

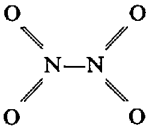

boron trichloride BCl_3,
boron tribromide BBr_3, and
boron triiodide BI_3.

The results are given in Table 2 and Figs. 10 and 11.

Octupolar molecules

The molecular models 3*a*–3*c* shown in Fig. 12 represent the crystal structures of octupolar molecules:

hexamethylenetetramine $(CH_2)_6N_4$,

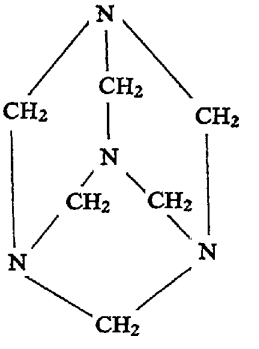

silicon tetrafluoride SiF_4,
silicon tetraiodide SiI_4, *etc.* and
tetraboron tetrachloride B_4Cl_4.

The results are given in Table 3 and Figs. 13–15.

In solid methane (melting point 90° K), two second-order transitions have been observed at 20·4 and 8° K. The structure between 20·4 and 90° K and that between 8 and 20·4° K is face-centred cubic (Schallamach, 1939). For tetradeuteromethane the transition temperatures are 27·1 and 22·4° K. A conclusion reached by Gissler & Stiller (1965) is that the structure below 22·4° K is probably neither cubic nor tetragonal.

The molecule of CH_4 and CD_4 is like the model 3*c* or the model 3*d*, each of which is a rounded tetrahedron. The model 3*c* forms four structures: cubic *Pa*3, tetragonal $P4_2/nmc$, tetragonal $I\bar{4}2m$, and monoclinic $C2/c$ (Figs. 14 and 15). The model 3*d* forms three: tetragonal $P4_2/nmc$, tetragonal $I\bar{4}2m$, and orthorhombic *Pban* (Figs. 16 and 17).

It is probable that the crystal structures of the lowest-temperature form of CH_4 and CD_4 are among these. If the crystal structure of CD_4 below 22·4° K is neither cubic nor tetragonal, then it will be either the orthorhombic *Pban* structure or the monoclinic $C2/c$ structure. As regards CH_4 below 8° K, the tetragonal $I\bar{4}2m$ structure is the most probable, because, when the temperature is raised, it may become a face-centred cubic structure in a straightforward way, the ratio c/a

decreasing from 1·8 to $\sqrt{2}$. It should be noted that this tetragonal structure was proposed by James & Keenan (1959) and Yamamoto (1968) in their theoretical analyses.

Molecules in the shape of a cube, an octahedron, or a trigonal bipyramid

The hexadecapolar models 4*a*–4*e* shown in Fig. 18 represent the crystal structures of molecules in the shape of a cube, an octahedron or a trigonal bipyramid: octa(silsesquioxane) $(HSi)_8O_{12}$,

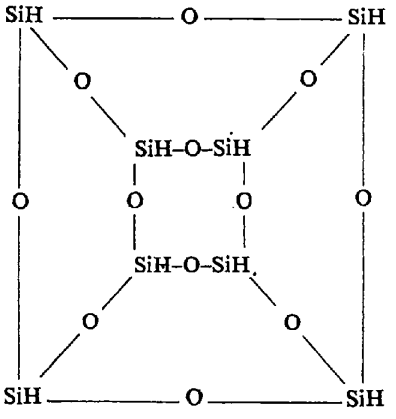

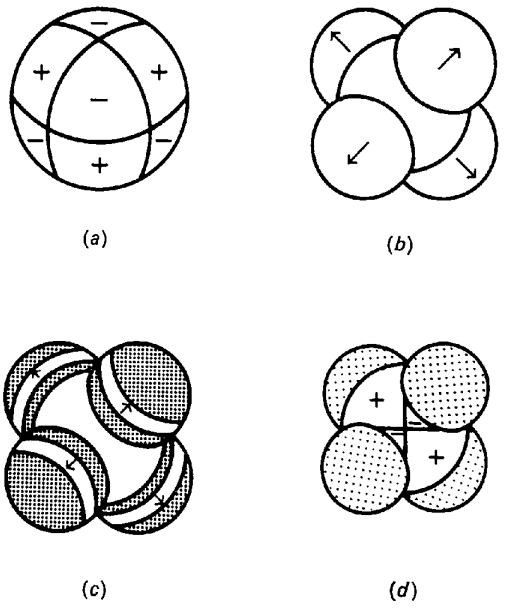

Fig. 12. Models of octupolar molecules. (*a*) Model 3*a*, octupolar sphere. (*b*) Model 3*b* for SiF_4; the central part is made of wood. (*c*) Model 3*c* for SiI_4, SnI_4, *etc.* (*d*) Model 3*d*, a rounded tetrahedron made of four Mn–Zn ferrite caps attached to an octupolar sphere. The Mn–Zn ferrite is the same as in (*c*).

Table 2. *Flat molecules*

β-$C_6H_6Cl_6$	$Pa3$ (T_h^6)	$Z=4$				(C.D.)
β-$C_6H_6Br_6$	$Pa3$ (T_h^6)	$Z=4$				(C.D.)
model 2*a*	$Pa3$ (T_h^6)	$Z=4$				Part II
C_6H_6	$Pbca$ (D_{2h}^{15})	$Z=4$	$b/a=0{\cdot}728$	$c/a=0{\cdot}772$ (−3 °C)		(C.D.)
model 2*b*	$Pbca$ (D_{2h}^{15})	$Z=4$	$b/a=0{\cdot}8$	$c/a=0{\cdot}9$		Part II
naphthalene	$P2_1/c$ (C_{2h}^5)	$Z=2$	$a/b=1{\cdot}35$	$c/b=1{\cdot}37$	$\beta=116°$	(C.D.)
anthracene	$P2_1/c$ (C_{2h}^5)	$Z=2$	$a/b=1{\cdot}56$	$c/b=1{\cdot}42$	$\beta=103°$	(C.D.)
$(CN)_2C=C(CN)_2$	$P2_1/c$ (C_{2h}^5)	$Z=2$	$a/b=1{\cdot}13$	$c/b=1{\cdot}75$	$\beta=137°$	(XIV, b25)
model 2*c*	$P2_1/c$ (C_{2h}^5)	$Z=2$	$a/b=1{\cdot}0$	$c/b=1{\cdot}4$	$\beta=120°$	Part II
N_2O_4	$Im3$ (T_h^5)	$Z=6$				(IV, i4)
model 2*d*	$Im3$ (T_h^5)	$Z=6$				Fig. 10
BCl_3	$P6_3/m$ (C_{6h}^2) or $P6_3$ (C_6^6)	$Z=2$		$c/a=1{\cdot}077$		(V, b16)
BBr_3	$P6_3/m$ (C_{6h}^2) or $P6_3$ (C_6^6)	$Z=2$		$c/a=1{\cdot}071$		(V, b16)
BI_3	$P6_3/m$ (C_{6h}^2) or $P6_3$ (C_6^6)	$Z=2$		$c/a=1{\cdot}066$		(V, b16)
model 2*e*	$P6_3/m$ (C_{6h}^2)	$Z=2$		$c/a=0{\cdot}94$		Fig. 11

Table 3. *Octupolar molecules*

$(CH_2)_6N_4$	$I\bar{4}3m$ (T_d^3)	$Z=2$				(C.D.)
model 3*a*	$I\bar{4}3m$ (T_d^3)	$Z=2$				Part II
SiF_4	$I\bar{4}3m$ (T_d^3)	$Z=2$				(V, c1)
model 3*b*	$I\bar{4}3m$ (T_d^3)	$Z=2$				Fig. 13
SiI_4, GeI_4, SnI_4, $TiBr_4$, TiI_4, $ZrCl_4$, $ZrBr_4$ and HfI_4	$Pa3$ (T_h^6)	$Z=8$				(V, c5)
B_4Cl_4	$P4_2/nmc$ (D_{4h}^{15})	$Z=2$	$c/a=0{\cdot}674$			(III, h7)
$P_4(CF_3)_4$	$P4_2/nmc$ (D_{4h}^{15})	$Z=2$	$c/a=0{\cdot}633$			(XIV, a41)
model 3*c*	$Pa3$ (T_h^6)	$Z=8$				Fig. 14
	$P4_2/nmc$ (D_{4h}^{15})	$Z=2$	$c/a=0{\cdot}71$			Fig. 15
	$I\bar{4}2m$ (D_{2d}^{11})	$Z=2$	$c/a=1{\cdot}8$			
	$C2/c$ (C_{2h}^6)	$Z=4$	$a/b=2{\cdot}2$	$c/b=2{\cdot}0$	$\beta=110°$	
model 3*d*	$P4_2/nmc$ (D_{4h}^{15})	$Z=2$	$c/a=0{\cdot}75$			
	$I\bar{4}2m$ (D_{2d}^{11})	$Z=2$	$c/a=1{\cdot}8$			Fig. 16
	$Pban$ (D_{2h}^4)	$Z=2$	$a/b=0{\cdot}55$	$c/b=0{\cdot}55$		Fig. 17

Fig. 15. Tetragonal $P4_2/nmc$ structure simulating the crystal structure of B_4Cl_4 (model 3*c*).

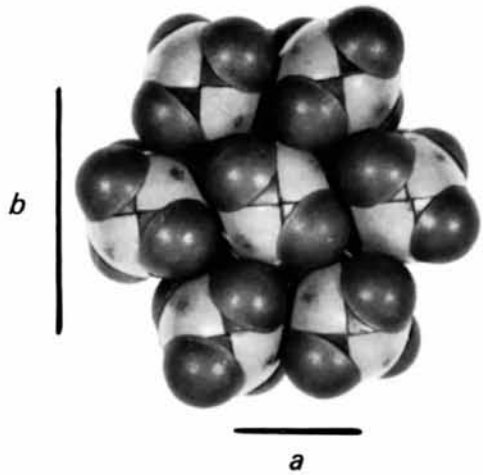

Fig. 17. Orthorhombic *Pban* structure (model 3*d*).

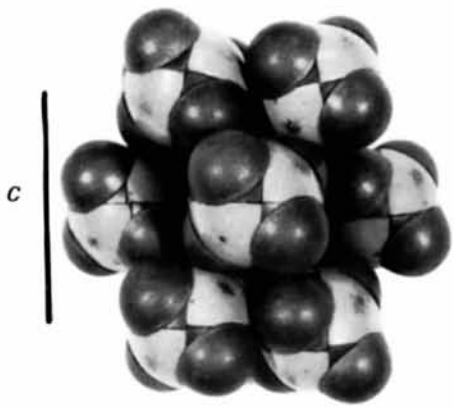

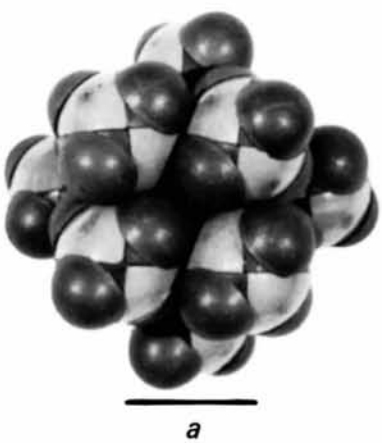

Fig. 16. Tetragonal $I\bar{4}2m$ structure (model 3*d*).

Fig. 19. Rhombohedral $R\bar{3}$ structure simulating the crystal structure of $(HSi)_8O_{12}$ and $(CH_3Si)_8O_{12}$ (model 4*a*).

[*To face p.* 318

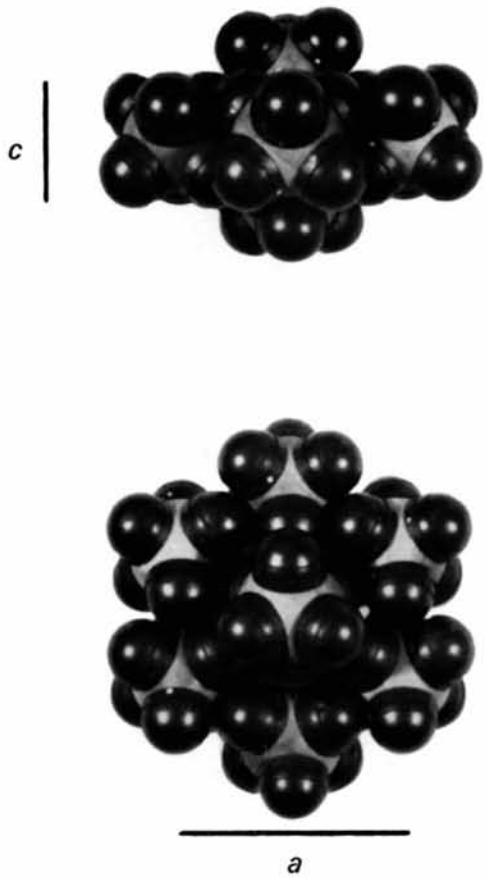

Fig. 20. Trigonal $P\bar{3}m1$ structure simulating the crystal structure of UCl_6 (model 4*c*).

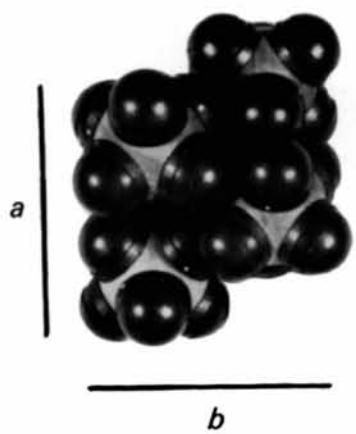

Fig. 21. Orthorhombic *Pnma* structure simulating the crystal structure of UF_6 (model 4*c*).

Fig. 22. Cubic $Fd3m$ structure or diamond structure simulating the crystal structure of As_4O_6 and Sb_4O_6 (model 4*d*).

Fig. 23. Hexagonal $P6_3/mmc$ structure simulating the crystal structure of $SbCl_5$ (model 4*e*).

octa(methylsilsesquioxane) $(CH_3Si)_8O_{12}$,
tungsten hexachloride WCl_6,
uranium hexachloride UCl_6,
uranium hexafluoride UF_6,
hexabromoethane C_2Br_6,
hexachloroethane C_2Cl_6 below 45°C,
tetraarsenic hexaoxide(arsenolite) As_4O_6,
tetraantimony hexaoxide(senarmontite) Sb_4O_6, and
antimony pentachloride $SbCl_5$.
The results are given in Table 4 and Figs. 19–23.

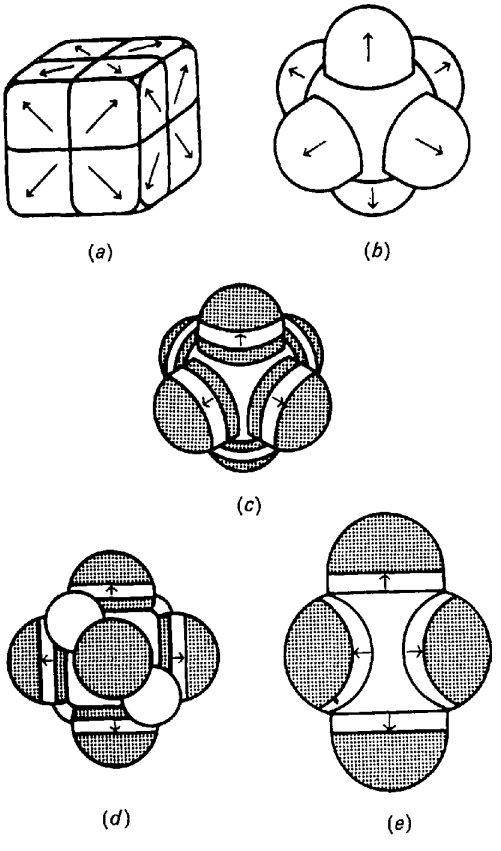

Fig. 18. Models of cube-like and octahedron-like molecules. (*a*) Model 4*a*, a hexadecapolar cube. (*b*) and (*c*) Models 4*b* and 4*c* for WCl_6, UCl_6, *etc.* (*d*) Model 4*d* for As_4O_6 and Sb_4O_6; the small spheres representing the atoms of As or Sb are made of wood. (*e*) Model 4*e* for $SbCl_5$.

The crystal structure of osmium octafluoride OsF_8 is probably the rhombohedral $R\bar{3}$ structure (Fig. 19) represented by the model 4*a*.

The crystal structures of ethane C_2H_6 and diborane B_2H_6 are reported to be

$$P6_3/mmc\ (D_{6h}^4)\ Z=2,\ c/a=1{\cdot}84 \text{ and } 1{\cdot}91$$

with respect to the positions of the carbon and boron atoms, respectively. If the positions of the hydrogen atoms are taken into account, the space group at low temperatures is probably $P\bar{3}1c$ (D_{3d}^2); this structure corresponds to

$$P\bar{3}1c\ (D_{3d}^2)\ Z=2,\ c/a=1{\cdot}89\,,$$

represented by the model 4*c*.

References

Bottger, G. L. & Eggers, J. (1964). *J. Chem. Phys.* **40**, 2010.

Donnay, J. D. H., Donnay, G., Cox, E. G., Kennard, O. & King, M. V. (1963). *Crystal Data.* 2nd ed. American Crystallographic Association.

Gissler, W. & Stiller, H. (1965). *Naturwissenschaften*, **52**, 512.

Ito, M., Yokoyama, T. & Suzuki, M. (1969). To be published.

Table 4. *Molecules in the shape of a cube, an octahedron, or a trigonal bipyramid*

$(HSi)_8O_{12}$	$R\bar{3}$ (C_{3i}^2)	$Z=1$	$\alpha=76°50'$		(C.D.)
$(CH_3Si)_8O_{12}$	$R\bar{3}$ (C_{3i}^2)	$Z=1$	$\alpha=95°39'$		(XIV, a62)
model 4*a*	$R\bar{3}$ (C_{3i}^2)	$Z=1$	$\alpha=100°$		Fig. 19
WCl_6	$R\bar{3}$ (C_{3i}^2)	$Z=1$	$\alpha=55°0'$		(V, f2)
UCl_6	$P\bar{3}m1$ (D_{3d}^3)	$Z=3$	$c/a=0{\cdot}551$		(V, f3)
UF_6	$Pnma$ (D_{2h}^{16})	$Z=4$	$b/a=0{\cdot}905$	$c/a=0{\cdot}526$	(V, f4)
C_2Br_6	$Pnma$ (D_{2h}^{16})	$Z=4$	$b/a=0{\cdot}887$	$c/a=0{\cdot}557$	(XIV, b7)
C_2Cl_6 below 45°C	$Pnma$ (D_{2h}^{16})	$Z=4$	$b/a=0{\cdot}881$	$c/a=0{\cdot}555$	(XIV, b7)
models 4*b* and 4*c*	$R\bar{3}$ (C_{3i}^2)	$Z=1$	$\alpha=53°$		Part I
models 4*b* and 4*c*	$P\bar{3}1c$ (D_{3d}^2)	$Z=2$	$c/a=1{\cdot}89$		Part I
models 4*b* and 4*c*	$P\bar{3}m1$ (D_{3d}^3)	$Z=3$	$c/a=0{\cdot}55$		Fig. 20
models 4*b* and 4*c*	$Pnma$ (D_{2h}^{16})	$Z=4$	$b/a=0{\cdot}92$	$c/a=0{\cdot}53$	Fig. 21
As_4O_6	$Fd3m$ (O_h^7)	$Z=8$			(V, a11)
Sb_4O_6	$Fd3m$ (O_h^7)	$Z=8$			(V, a11)
model 4*d*	$Fd3m$ (O_h^7)	$Z=8$			Fig. 22
$SbCl_5$	$P6_3/mmc$ (D_{6h}^4)	$Z=2$	$c/a=1{\cdot}069$		(V, e4)
model 4*e*	$P6_3/mmc$ (D_{6h}^4)	$Z=2$	$c/a=1{\cdot}4$		Fig. 23

Erratum: The space group for UCl_6 should read $P\bar{3}m1$, not $P\bar{3}1m$, in part I.

JAMES, H. M. & KEENAN, T. A. (1959). *J. Chem. Phys.* **31**, 12.
KIHARA, T. (1963). *Acta Cryst.* **16**, 1119.
KIHARA, T. (1966). *Acta Cryst.* **21**, 877.
SCHALLAMACH, A. (1939). *Proc. Roy. Soc.* A**171**, 569.
SUGAWARA, T. & KANDA, E. (1952). *Sci. Rep. R.I. Tohoku Univ. (Japan)*, A**4**, 607.
WYCKOFF, R. W. G. (1963). *Crystal Structures*, 2nd ed. Vol. 1. New York: John Wiley.
WYCKOFF, R. W. G. (1964). *Crystal Structures*, 2nd ed. Vol. 2. New York: John Wiley.
WYCKOFF, R. W. G. (1966). *Crystal Structures*, 2nd ed. Vol. 5. New York: John Wiley.
YAMAMOTO, T. (1968). *J. Chem. Phys.* **48**, 3193.

Acta Cryst. (1970). A**26**, 320

Untersuchung über die Begrenzung röntgenographisch ermittelter Teilchengrössen

VON RENATE STERZEL UND W. STERZEL

Institut für anorganische Chemie der Universität Frankfurt, Deutschland

(*Eingegangen am* 25. *November* 1968 *und wiedereingereicht am* 8. *April* 1969)

Changes of particle size and strain during annealing of cold-worked aluminum powders have been determined by measuring X-ray line breadths. Aluminum powders ground under special conditions show a decrease in particle size as well as a reduction of strains within certain ranges of temperature. This is due to polygonization processes and allows conclusions to be drawn regarding the limits of coherent regions of X-ray diffraction. The X-ray measurements were supplemented by electron microscope studies.

1. Bestimmung von Teilchengrössen und Gitterverzerrungen aus Linienbreiten

Breite und Form der Beugungslinien in Röntgendiagrammen werden durch die Abweichungen der reflektierenden Kristallteilchen vom idealen Gitterbau beeinflusst. Auf Grund der unterschiedlichen Abhängigkeit vom Braggschen Beugungswinkel kann die Verbreiterung durch kleine Teilchen von der durch Gitterverzerrungen getrennt werden. Für diese Trennung sind allerdings Annahmen über die Verteilungsfunktionen der Teilchengrössen und Gitterverzerrungen erforderlich. Obwohl die röntgenographisch ermittelten Grössen für die Beurteilung des Störungsgrades eines Materials und besonders für den Vergleich von Präparaten sehr wertvoll sind, ist nur sehr wenig über die reale Bedeutung der gewonnenen röntgenographischen Teilchengrössen bekannt.

Bei der Einführung des Teilchengrössenbegriffs in diesem Zusammenhang durch Scherrer (1918) wurde davon ausgegangen, dass ein Präparat aus Bereichen besteht, innerhalb derer eine kohärente Beugung der Röntgenstrahlung erfolgt und die bezüglich der Interferenz der Strahlung klar voneinander getrennt sind. Im realen Material gibt es jedoch alle Übergänge zwischen völlig getrennten Kristallteilchen und Bereichen, die auf Grund einzelner Versetzungen nur sehr geringe Orientierungsunterschiede aufweisen.

Williamson & Hall (1953) kamen bei der Untersuchung von verformten Metallen zu der Ansicht, dass man als röntgenographische Teilchengrösse bei der Auswertung von Linienbreiten den mittleren Abstand der Versetzungslinien erfasst. In einer späteren Arbeit von Williamson & Smallman (1956) wird diese Vorstellung etwas modifiziert und nur im stark verformten und im weitgehend rekristallisierten Zustand werden unregelmässig verteilte Versetzungen angenommen, deren mittlerer Abstand die röntgenographische Teilchengrösse ergibt.

Eigene Untersuchungen an stark verformten Aluminiumpulvern ergaben, dass für einige Präparate in gewissen Bereichen der Erholung die aus den Integralbreiten der Röntgenbeugungslinien ermittelten Teilchengrössen beim Erhitzen abnehmen. Diese Teilchengrössenabnahme erfolgt bei gleichzeitigem Rückgang der gemessenen Gitterverzerrungen. Die genaue Bestimmung der Teilchengrössen und Gitterverzerrungen einer Reihe stark verformter Präparate bei möglichst vielen Stufen der Rekristallisation versprach deshalb neue Informationen über die Begrenzung der röntgenographischen Kohärenz in polykristallinem Material.

2. Die verwendeten Aluminiumpräparate

Die untersuchten Aluminiumpulver wurden durch Mahlen in einer Kugelmühle aus einem Material hoher Reinheit gewonnen. Durch den Mahlprozess, der in verschiedenen Mahlflüssigkeiten unter Edelgasatmosphäre mit dosierten Sauerstoffanteilen erfolgte, wurden feinteilige Aluminiumpulver mit sehr hohem Störungsgrad erhalten. Nach Untersuchungen von Royen & Romeis (1962) sind in solchen Aluminiumpulvern die Gitterstörungen durch eingemahlene Oxidteilchen bzw. durch die Oxidbedeckung der Oberflächen stabilisiert, und die Rekristallisation ist auch bei höheren Temperaturen stark gehemmt.